communications physics

ARTICLE

https://doi.org/10.1038/s42005-021-00590-8 OPEN

Reciprocating propagation of laser pulse intensity in free space

Zhaoyang Li [1✉], Yanjun Gu [1] & Junji Kawanaka [1]

Constant-speed straight-line propagation in free space is a basic characteristic of light, and spatiotemporal couplings recently were used to control light propagation. In the method of flying focus, where temporal chirp and longitudinal chromatism were combined, tunable-velocities and even backward-propagation were demonstrated. We studied the transverse and longitudinal effects of the flying focus in space-time and found in a specific physics interval existing an unusual reciprocating propagation that was quite different from the previous result. By increasing the Rayleigh length in space and the temporal chirp in time, the created flying focus can propagate along a longitudinal axis firstly forward, secondly backward, and lastly forward again, and the longitudinal spatial resolution improves with increasing the temporal chirp. When this light is applied in a radiation pressure simulation, a reciprocating radiation-force can be produced accordingly. This finding extends the control of light and might enable important potential applications.

[1] Institute of Laser Engineering, Osaka University, Suita, Osaka, Japan. ✉email: zhaoyang-li@ile.osaka-u.ac.jp

Optical pulse propagation, including velocity and direction, is a very basic characteristic for applications like optical information/communication, laser-matter interaction, and so on[1–6]. In linear physics, an optical pulse propagates along a straight-line trajectory at the group velocity of c/n_g, where c is the speed of light in the vacuum and n_g is the group refractive index in the medium. In this case, the propagating velocity and/or direction can be controlled by crafting the spectrum- and space-dependent refractive index $n_\lambda(x, y, z)$[7–12]. However, this kind of method cannot be directly applied in free space, where the refractive index is constant $n = 1$. Another approach is by shaping beam in space or pulse in time to change the propagating velocity (e.g., superluminal or accelerating velocity) and direction (e.g., straight-line or bended trajectory) in free space[13–23]. For example, a Bessel beam can propagate along a straight-line trajectory at a superluminal velocity governed by $c/\cos\alpha$ in free space, where α is the half conical angle of the conical superposition[13,14]; an Airy beam can propagate along a parabolic trajectory at an accelerating superluminal group velocity in free space[15–22]; an Airy-Bessel pulsed beam (called light bullet) can propagate along a straight-line trajectory at an accelerating superluminal group velocity in a dispersion medium[23].

Currently, spatiotemporal (ST) couplings are frequently used to modulate the propagation or structure of a pulsed beam, which permits both velocity control (i.e., superluminal or subluminal, and accelerating or decelerating) and direction control (i.e., forward or backward)[24–38]. The first example is the three-dimensional (3-D) flying focus (FLFO) within the extended Rayleigh length independently demonstrated by Quéré, et al.[24,25] (originally named "sliding focus") and Froula et al.[26,27] (originally named "flying focus"), respectively, which can propagate at an arbitrary group velocity in free space including all motion forms of superluminal or subluminal, accelerating or decelerating, and forward or backward propagations. The second example is the two-dimensional (2-D) optical ST wave-packet demonstrated by Abouraddy et al.[28–34], which can also propagate at an arbitrary group velocity in free space, including all above motion forms. The third example is the 3-D ST Gauss-Bessel pulsed-beam (or 3-D optical wave-packet) created by pre-deforming the pulse-front of the input Gauss pulsed-beam that is for the generation of a Gauss-Bessel pulsed-beam[35,36], similarly whose group velocity is tunable, too. Apart from the above motion forms (i.e., superluminal or subluminal, accelerating or decelerating, and forward or backward propagations), a compound motion with several different motion forms in a single propagation path is also possible[36].

In the above methods, we can find that the created optical pulse/wave-packet can only propagate towards one certain direction (i.e., forward or backward), although the propagating velocity (i.e., superluminal or subluminal, and accelerating or decelerating) and trajectory (i.e., straight-line or bend) can be well controlled. In this article, we report a phenomenon of a reciprocating FLFO, whose motion form includes three steps: forward-propagation firstly, backward-propagation secondly, and forward-propagation again lastly. For the FLFO created by longitudinal chromatism and temporal chirp[24,26], whose group velocity within the extended Rayleigh length has been well studied under the geometrical optics, however, the influence of the Rayleigh length as determined by the F-number is not well considered.

Here, we significantly increase the Rayleigh length with respect to the focus-separation induced by longitudinal chromatism and then compare the propagating dynamics of the FLFO with the previous case. The result shows, the FLFO experiences a forward-backward-forward reciprocating propagation from the appearance to the disappearance. This motion form of the reciprocating FLFO may bring potentials in applications like particle manipulation, laser acceleration, radiation generation, and so on. In this article, we took the nanoparticle ultrafast trapping or manipulation as an example and analyzed the ST-variable radiation-force induced by this reciprocating FLFO, which may bring opportunities to this field.

Results and discussion

Generation mechanism. Figure 1a shows the schematic of the FLFO that frequently appears in an ultrafast optical experiment. Before the focusing optics, the pulse duration is stretched by a dispersion element (e.g., grating pair, bulk material or fiber, etc.) with temporal chirp in time, and the spectrum-dependent wavefronts are deformed by a chromatic element [e.g., confocal (only for the center frequency) transmission telescope] with longitudinal chromatism in space (two elements are not shown in Fig. 1a). As illustrated in Fig. 1a, the low-frequency component is flying at the temporal leading edge and is focused onto the location far away from the focusing optics, vice versa. The propagation of this FLFO has already been well studied, and the velocity equation has been derived by Quéré, et al.[24,25] and Froula et al.[26,39] independently. If based on geometrical optics and linear approximation, the velocity equation can be simplified as

$$v_{\mathrm{FLFO}} \approx \frac{-L_f}{L_c - L_f} c \tag{1}$$

with

$$L_f = 2cf^2\alpha\frac{\Delta\omega}{\omega_0} \tag{2}$$

$$L_c = -\phi_2\Delta\omega c \tag{3}$$

where, L_f and L_c are total focus-separation and total pulse-separation (corresponding to the pulse bandwidth $\Delta\omega$) on the propagation axis induced by longitudinal chromatism and temporal chirp, respectively, f is the focal length of the focusing optics, α is a parameter describing the pulse-front curvature (PFC) or named radial group delay (RGD) of $\mathrm{GD}(r) = \alpha r^2$ in the near-field induced by longitudinal chromatism[24,25], c is the light-speed in free space, ω_0 is the center frequency, and ϕ_2 is the group-velocity dispersion (GVD). It is important to note that L_f and L_c have directions, which are defined from the lowest-frequency ("red" light) to the highest frequency ("blue" light) on the propagation axis. The derivations of Eqs. (1), (2), and (3) are given in Supplementary Information Notes 3, 2, and 1, respectively. When $L_c/L_f > 1$ (i.e., $L_c < L_f < 0$ for the case of positive temporal chirp $\phi_2 > 0$ and concave PFC $\alpha < 0$ that is the case in this article, or $L_c > L_f > 0$ for the case of negative temporal chirp $\phi_2 < 0$ and convex PFC $\alpha > 0$), the result of Eq. (1) is negative, showing a backward-propagating FLFO [see Fig. 1d]. The mechanism of the FLFO velocity control is that the longitudinal chromatism spatially separates the frequency-dependent foci on the propagation axis and the temporal chirp temporally controls the time of every frequency arriving at its focus, resulting in a moving pulse-intensity-peak (i.e., FLFO). Figure 1b schematically shows: at time t_1, both low- and high-frequencies are before their geometrical foci, and no FLFO exists; at time t_2, the low-frequency arrives at its geometrical focus, while the high-frequency does not (due to $L_c < L_f < 0$), and the FLFO appears at the ST position of the low-frequency; at time t_3, the low-frequency has passed through its geometrical focus, while the high-frequency is now at its geometrical focus (due to $L_c < L_f < 0$), and the FLFO flies backwards to the ST position of the high-frequency; finally at time t_4, both low- and high-frequencies have passed through their geometrical foci, and the FLFO disappears.

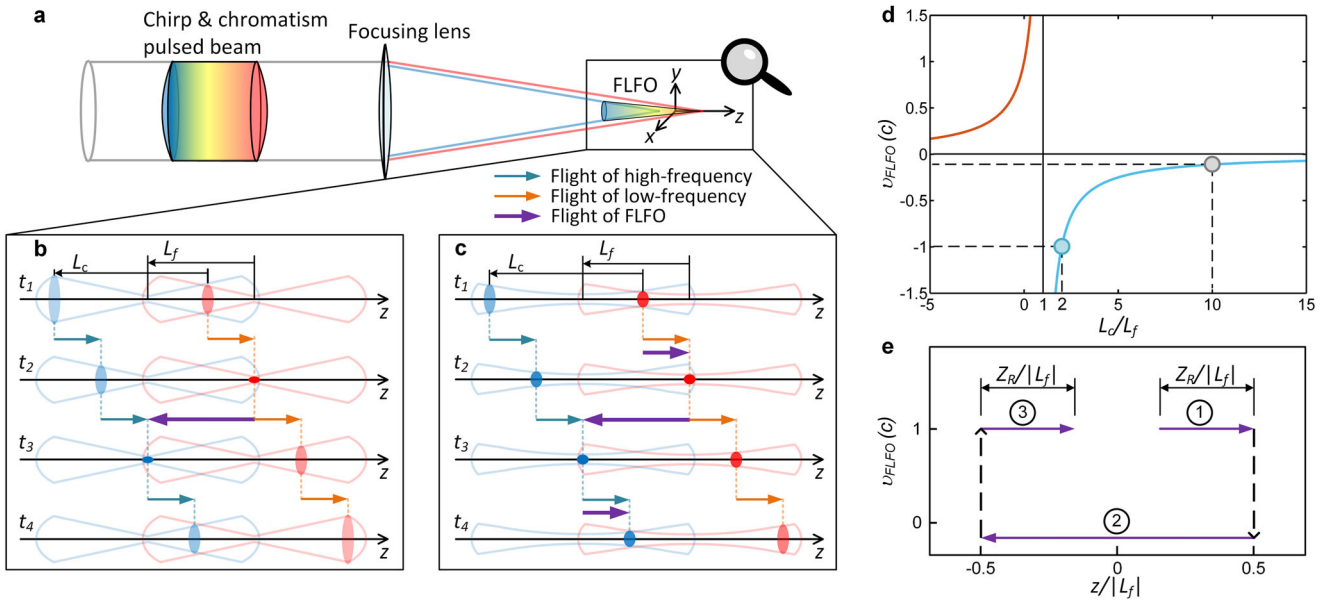

Fig. 1 Generation mechanism and characteristic of reciprocating FLFO. a Flying focus (FLFO) is formed by coupling of longitudinal chromatism and temporal chirp within an extended Rayleigh length. Longitudinal chromatism separates frequency-dependent foci in space, and temporal chirp controls moments of frequencies arriving at their foci in time, resulting in a moving pulse-intensity-peak, i.e., a velocity tunable FLFO. **b** Typical backward-propagating FLFO with short Rayleigh lengths, at time t_1 all frequencies are before their foci; at time t_2 low-frequency arrives at its focus, while high-frequency does not; at time t_3 high-frequency arrives at its focus, while low-frequency leaves its focus; at time t_4 all frequencies leave their foci. FLFO moves backwards from the focus of low-frequency to that of high-frequency from time t_2 to t_3. L_c and L_f are temporal chirp and longitudinal chromatism induced on-axis pulse-separation and focus-separation corresponding to the pulse bandwidth, respectively. Here $L_c < L_f < 0$ (along the negative direction of the z-axis) with positive temporal chirp and concave pulse-front curvature, i.e., low-frequency locates at the temporal leading edge and has a long focal length. **c** Reciprocating FLFO with enlarged Rayleigh lengths, at time t_1 low-frequency enters its Rayleigh length, while high-frequency does not; at time t_2 low-frequency arrives at its geometrical focus, while high-frequency does not; at time t_3 high-frequency arrives at its geometrical focus, while low-frequency leaves its geometrical focus; at time t_4 high-frequency is still in its Rayleigh length, while low-frequency leaves its Rayleigh length. FLFO moves forwards within the low-frequency's Rayleigh length from time t_1 to t_2, backwards from the geometrical focus of low-frequency to that of high-frequency from time t_2 to t_3, and finally forwards again within the high-frequency's Rayleigh length from time t_3 to t_4. **d** Group velocity of FLFO v_{FLFO} as a function of L_c/L_f. **e** On-axis location of reciprocating FLFO during ① forward-, ② backward-, and finally ③ forward-propagations with corresponding velocities v_{FLFO}. Z_R is the Rayleigh length, and lengths and positions are normalized by $|L_f|$.

During this process, all frequencies move forwards at the light-speed in free space c, but the FLFO flies backwards at the velocity governed by Eq. (1), which can be superluminal or subluminal. Figure 1d shows the dependence of the velocity of this FLFO with the temporal chirp induced pulse-separation L_c that is normalized by the longitudinal chromatism induced focus-separation L_f.

In the above typical FLFO, the Rayleigh length $Z_R(\omega)$ comparing with the longitudinal chromatism induced focus-separation L_f is very short and negligible [see Fig. 1b]. When dramatically increasing the Rayleigh length $Z_R(\omega)$ by reducing the beam diameter (or numerical aperture, NA) at the focusing optics, the typical backward-propagating FLFO is changed into a reciprocating FLFO. Figure 1c schematically shows: at time t_1, the low-frequency is before its geometrical focus but has entered its Rayleigh length, while the high-frequency does not, showing a forward-propagating FLFO; from time t_2 to t_3, it becomes the typical backward-propagating FLFO; at time t_4, the high-frequency has passed through its geometrical focus but is still within its Rayleigh length, while the low-frequency does not, showing a forward-propagating FLFO again. The result is the FLFO has a reciprocating motion on the propagation axis. When the origin of the propagation axis (z-axis) is defined at the midpoint of L_f (i.e., the geometrical focus of the center frequency ω_0 for linear longitudinal chromatism), Fig. 1e shows the propagation of the reciprocating FLFO is divided into three steps: firstly, forward-propagation from $z = |L_f|/2 - Z_R$ to $z = |L_f|/2$; secondly, backward-propagation from $z = |L_f|/2$ to $z = -|L_f|/2$; thirdly, forward-propagation from $z = -|L_f|/2$ to $z = -|L_f|/2 + Z_R$. The two forward-propagations have a constant velocity c in free space, but the backward-propagation has a tunable velocity governed by Eq. (1) and shown by Fig. 1d. Here, because a limited bandwidth $\Delta\omega$ is considered, the frequency-dependence of the Rayleigh lengths $Z_R(\omega)$ is neglected, and then $Z_R(\omega)$ is represented by Z_R.

Numerical demonstration. The numerical demonstration is carried out by using the model given in the "Methods" section and the following parameters: the pulse has an 800 nm center wavelength and a 20 nm flat-top bandwidth; the focusing optics has a 400 mm (for the center wavelength 800 nm) focal length; the longitudinal chromatism is generated by a BK7 confocal (only for the center wavelength 800 nm) telescope $f_1 - f_2$ with a $L_f = -5$ mm focus-separation (from the longest wavelength 810 nm to the shortest wavelength 790 nm), when $f_1 = f_2 = 50$ mm (for the center wavelength 800 nm). The temporal chirp (i.e., L_c) is modulated for FLFOs with different velocities and longitudinal spatial resolutions, and the beam diameter is adjusted for different Rayleigh lengths Z_R. When the temporal chirp induced pulse-separation is $L_c = -10$ mm ($2L_f$) (from the longest wavelength 810 nm to the shortest wavelength 790 nm) and the Rayleigh length is $Z_R = 50$ μm ($0.01|L_f|$), Fig. 2a shows the time-integrated extended Rayleigh length within a 0.1 × 12 mm lateral region, and Fig. 2b gives the dynamics at different propagating

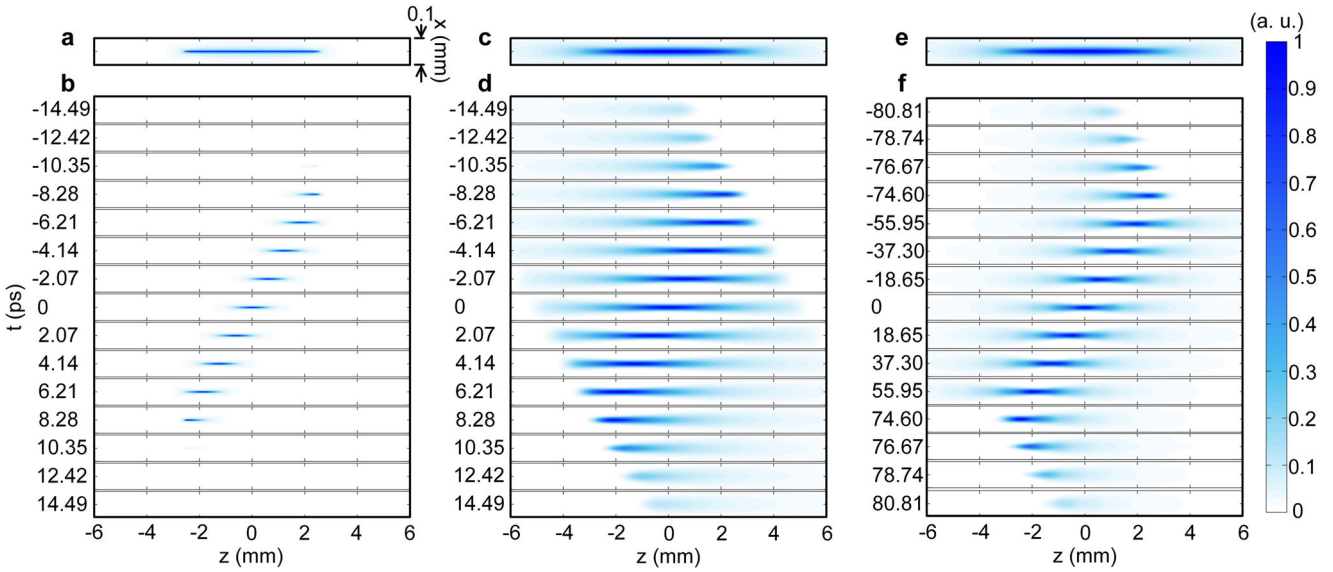

Fig. 2 Numerical demonstration and comparison. When **a**, **b** $Z_R = 0.01|L_f|$ & $L_c = 2L_f$, **c**, **d** $Z_R = 0.15|L_f|$ & $L_c = 2L_f$, and **e**, **f** $Z_R = 0.15|L_f|$ & $L_c = 10L_f$, **a**, **c**, **e** time-integrated extended Rayleigh length within a 0.1 × 12 mm 2-D lateral spatial region. **b**, **d**, **f** Dynamics of Flying focus (FLFO) within the same 2-D lateral spatial region at different propagating times t, showing **b** typical backward-propagating FLFO, **d** reciprocating FLFO, and **f** clear reciprocating FLFO, respectively. Intensity distributions are normalized by the maximum during the propagation and share the same color scale. Z_R is the Rayleigh length of the center frequency, L_c and L_f are temporal chirp and longitudinal chromatism induced on-axis pulse-separation and focus-separation corresponding to the pulse bandwidth (from 810 nm to 790 nm), respectively, and $L_f = -5$ mm.

times t, showing a typical backward-propagating FLFO. The propagating time t in this article is defined as $t = z/c$, and the time of the center frequency ω_0 (i.e., the FLFO for linear temporal chirp and linear longitudinal chromatism) arriving at the space origin $z = 0$ (i.e., the geometrical focus of the center frequency ω_0 for linear longitudinal chromatism) is defined as the propagating time origin $t = 0$. Keeping the temporal chirp unchanged, when the Rayleigh length is enlarged from 50 μm ($0.01|L_f|$) to 0.75 mm ($0.15|L_f|$) by reducing the beam diameter from 57.2 to 14.8 mm, Fig. 2c shows the time-integrated extended Rayleigh length is stretched and thickened. Figure 2d shows the corresponding dynamics at different propagating times t, and the reciprocating motion of the FLFO can be found. Next, keeping the enlarged Rayleigh length ($0.15|L_f|$) unchanged, when the temporal chirp induced pulse-separation L_c is enlarged from -10 mm ($2L_f$) to -50 mm ($10L_f$) by increasing the temporal chirp, the time-integrated extended Rayleigh length remains unchanged [see Fig. 2e], however, the longitudinal spatial resolution of the FLFO is enhanced, showing a clear reciprocating FLFO [see Fig. 2f]. Figure 2 indicates two results: first, increasing the Rayleigh length (by reducing NA) is necessary for the reciprocating FLFO [see Fig. 2d]; second, dramatically increasing the temporal chirp can enhance the longitudinal spatial resolution of the reciprocating FLFO [see Fig. 2f]. The previous results show a large temporal chirp would reduce the velocity of the backward-propagation. The blue and gray spots in Fig. 1d show the backward-propagating velocities in Fig. 2b/d and 2f are $-c$ and $-0.11c$, respectively, which is why the time interval during the backward-propagation in Fig. 2f is increased.

In summary, to generate a reciprocating FLFO: firstly, the temporal chirp induced pulse-separation should be longer than the longitudinal chromatism induced focus-separation $L_c/L_f > 1$ (i.e., $L_c < L_f < 0$ for the case of positive temporal chirp $\phi_2 > 0$ and concave PFC $\alpha < 0$ that is the case in this article, or $L_c > L_f > 0$ for the case of negative temporal chirp $\phi_2 < 0$ and convex PFC $\alpha > 0$), generating a typical backward-propagating FLFO; secondly, the Rayleigh length Z_R should be obviously enlarged $Z_R \gg 0$, showing obvious forward-propagating FLFOs before and after the backward-propagation; thirdly, the Rayleigh length should be shorter than the longitudinal chromatism induced focus-separation $|L_f| > Z_R > 0$, improving the longitudinal spatial resolution of the FLFO; finally, the temporal chirp should be significantly enhanced $L_c/L_f \gg 1$, further improving the longitudinal spatial resolution for a clear reciprocating FLFO. The requirement then becomes $|L_c| \gg |L_f| > Z_R \gg 0$ with $L_c/L_f > 0$.

Spectral effect. The above numerical demonstration is based on a flat-top spectrum. As the dynamics of the FLFO and the spectral profile of the pulse have a strong correlation, it is necessary to discuss the spectral effect. Keeping the parameters used in Fig. 2e, f unchanged, when the spectral profile is changed from flat-top into supper-Gaussian [see Fig. 3a], Fig. 3b, c show the time-integrated extended Rayleigh length and the dynamics of the FLFO at different propagating times t. The intensity and the ST position of the forward-propagating FLFOs before and after the backward-propagation are obviously reduced and slightly changed, respectively, which actually is caused by the "gentle" rising and falling edges of the spectrum. For observing the weak forward-propagating FLFOs, the color scale of Fig. 3 is adjusted. Next, when the spectral profile is changed into saddle-shape [see Fig. 3d], Fig. 3e shows the time-integrated extended Rayleigh length is insensitive to this change, however, Fig. 3f shows the dynamics of the FLFO at different propagating times t obviously change because the instantaneous FLFO corresponds to different frequencies at different propagating times/positions. When comparing Fig. 3c, f with Fig. 2f, "steep" rising and falling edges of the spectrum are also required for a clear reciprocating FLFO. Moreover, the propagating dynamics of the FLFO can be freely controlled by modulating the spectral profile, which has already been introduced in the previous work[26].

Existence of clear reciprocating FLFO. The analytical formulas given in the "Methods" section [see Eq. (18)] show the length (the full width at half maximum, FWHM) ΔL of the reciprocating FLFO is proportional to a product $M \cdot Z_R$, i.e., $\Delta L \propto M \cdot Z_R$, where

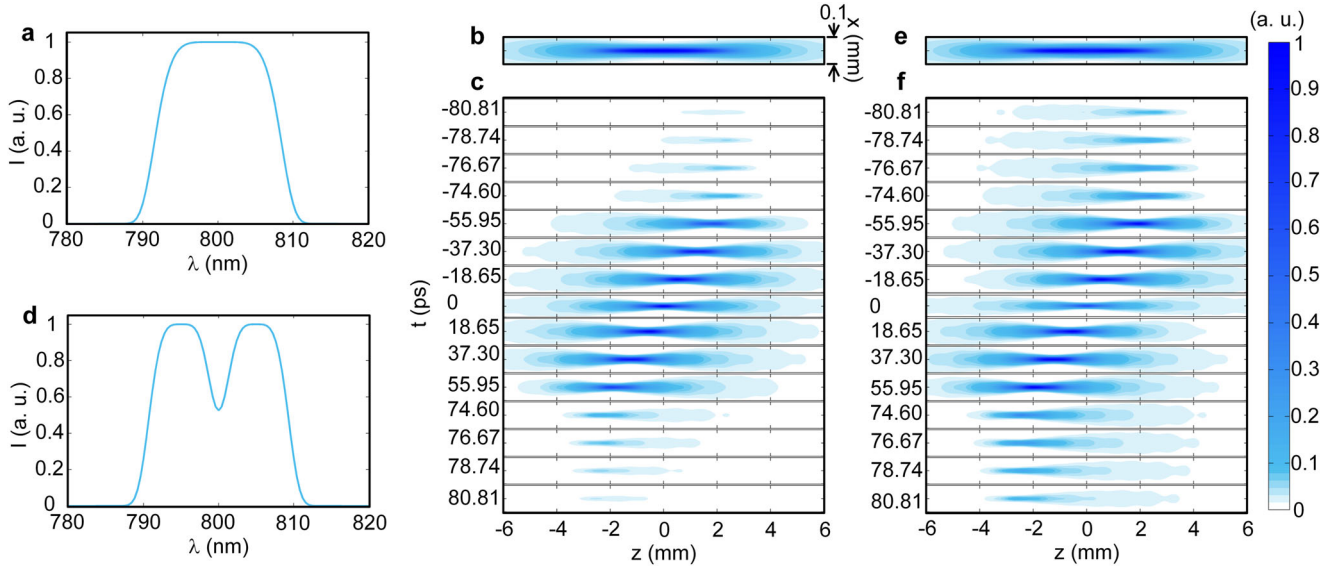

Fig. 3 Reciprocating FLFO with different spectra. When $Z_R = 0.15|L_f|$ & $L_c = 10L_f$, for **a**, **b**, **c** super-Gaussian and **d**, **e**, **f** saddle-shape spectra, **b**, **e** time-integrated extended Rayleigh length within a 0.1 × 12 mm 2-D lateral spatial region for super-Gaussian and saddle-shape spectra, respectively. **c, f** Dynamics of Flying focus (FLFO) within the same 2-D lateral spatial region at different propagating times t for super-Gaussian and saddle-shape spectra, respectively. Intensity distributions are normalized by the maximum during the propagation and share the same color scale. Z_R is the Rayleigh length of the center frequency, L_c and L_f are temporal chirp and longitudinal chromatism induced on-axis pulse-separation and focus-separation corresponding to the pulse bandwidth (from 810 nm to 790 nm), respectively, and $L_f = -5$ mm.

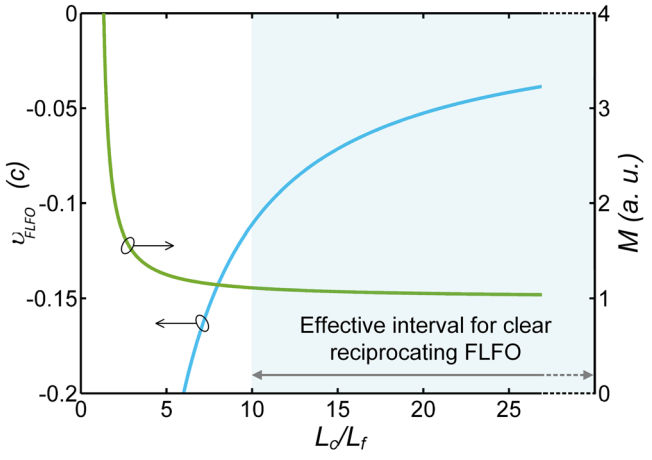

Fig. 4 Existence interval of clear reciprocating FLFO. Group velocity v_{FLFO} of backward-propagating Flying focus (FLFO) and parameter M as functions of L_c/L_f. The colored area shows the effective interval for a clear reciprocating FLFO, where the parameter M approaches infinitely to its minimum value 1. M equals $(L_c/L_f)/(L_c/L_f - 1)$ and is proportional to the length of the reciprocating FLFO, and L_c and L_f are temporal chirp and longitudinal chromatism induced longitudinal pulse-separation and focus-separation corresponding to the pulse bandwidth, respectively.

$M = L_c/(L_c - L_f)$. When the longitudinal spatial resolution of the FLFO is defined as the ratio between the FLFO length and the longitudinal chromatism induced focus-separation $R_{\mathrm{FLFO}} = \Delta L/L_f$, the longitudinal spatial resolution $R_{FLFO} \propto M{\cdot}Z_R/L_f$ improves with increasing the temporal chirp L_c (i.e., with reducing the parameter M), and this agrees well with the simulation results in Fig. 2d, f. Figure 4 shows the temporal chirp L_c/L_f (i.e., normalized by L_f) determines both the backward-propagating velocity v_{FLFO} and the longitudinal spatial resolution R_{FLFO} of the FLFO. When the normalized temporal chirp L_c/L_f is larger than 10 ($L_c/L_f = 10$ is the case in Fig. 2f), the parameter M approaches infinitely to its minimum value 1, where a clear reciprocating FLFO with the shortest length ΔL and the best longitudinal spatial resolution R_{FLFO} can be observed. However, the backward-propagating velocity of the FLFO is limited less than $0.11c$ in free space, which would further decrease with increasing the temporal chirp L_c/L_f. Noting that, the forward-propagating velocity of the FLFO will not be affected by adjusting the temporal chirp, which always is constant c in free space. Finally, the result is that a clear reciprocating FLFO exists in the interval of $L_c/L_f \in [10, \infty)$, where it has a $[-0.11c, 0)$ subluminal backward-propagating velocity and a light-speed c forward-propagating velocity in free space. This phenomenon can be found in the simulated dynamics as shown in Fig. 2f. Another parameter affecting the longitudinal spatial resolution R_{FLFO} of the reciprocating FLFO is the Rayleigh length Z_R, which generally cannot be too small (reducing the forward-propagation distance) or too large (degrading the longitudinal spatial resolution), and the simulation here indicates it is better to keep it within around $0.1|L_f| \sim 0.2|L_f|$.

Possible applications. The propagation form of the reciprocating FLFO provides a tool for laser pulse intensity control in space-time. For applications like optical trapping/manipulating/accelerating small particles with the laser radiation pressure developed by Ashkin et al., especially in biology, medicine, and nanoscience[40–44], the dynamic radiation-force induced by the reciprocating FLFO may bring some possibilities. In the Rayleigh-scattering regime where the particle is sufficiently smaller than the laser wavelength, Fig. 5a shows the radiation-force exerted on a small dielectric sphere (treated as an induced, simple point dipole) can be divided into two components: a scattering force $\mathbf{F_{scat}}$ and a gradient force $\mathbf{F_{grad}}$[43,45]. The scattering force $\mathbf{F_{scat}}$ is proportional to the product $a^6 I$ and points in the direction of the beam, and the gradient force $\mathbf{F_{grad}}$ is proportional to the product $a^3 \nabla I$ and points in the direction of the intensity gradient, where a is the radius of the sphere and I is the laser intensity. Recently, pulsed Gaussian beams also are used as optical tweezers, which can produce much stronger radiation-forces than those by

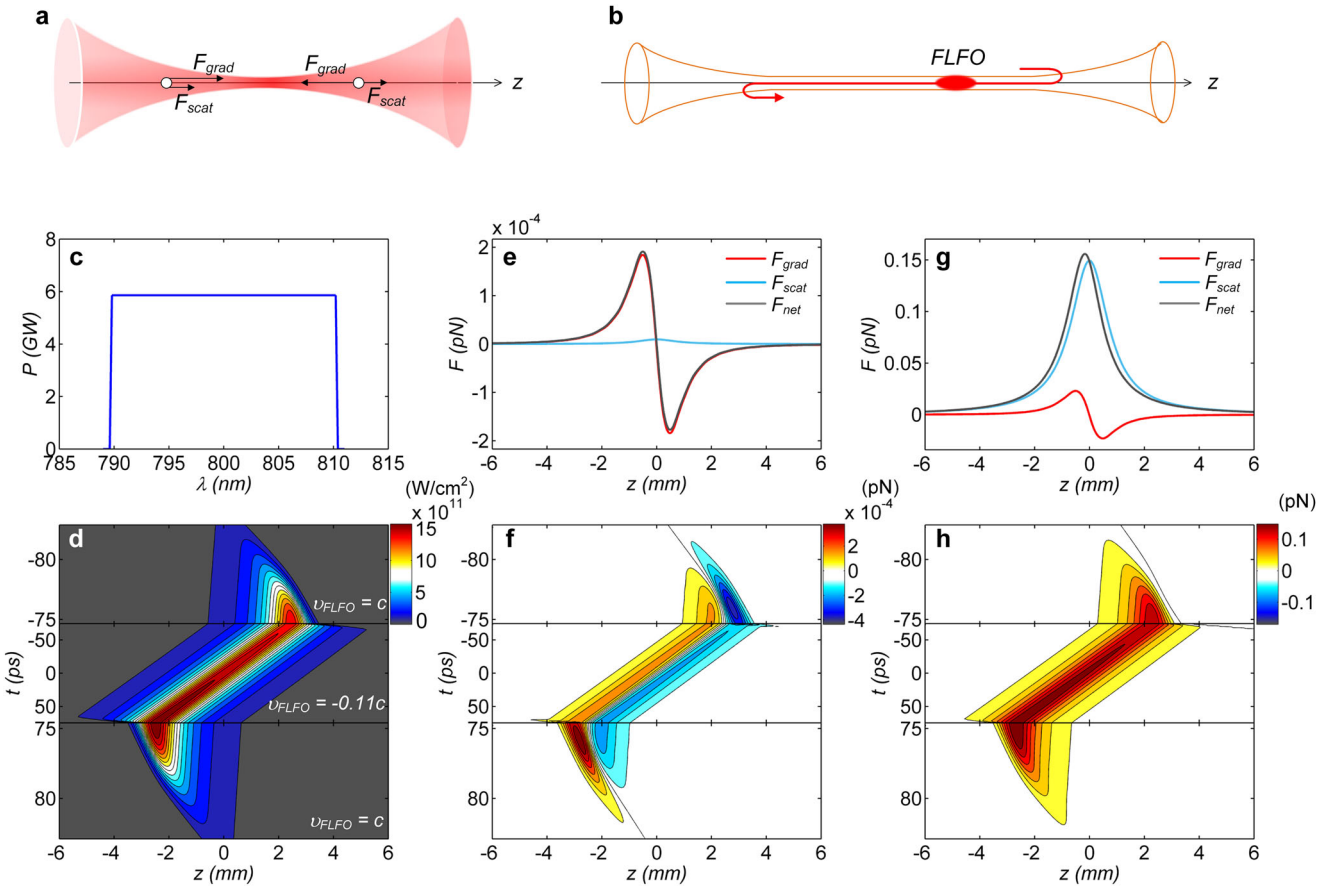

Fig. 5 Reciprocating FLFO induced radiation-forces. a Schematic of continuous-wave Gaussian laser beam radiating a Rayleigh dielectric sphere and induced longitudinal axial (*z*-axis) radiation-forces of scattering force $\mathbf{F_{scat}}$ and gradient force $\mathbf{F_{grad}}$. **b** Schematic of reciprocating Flying focus (FLFO) in an extended Rayleigh length, orange curve illustrates the beam profile, red curve illustrates the reciprocating motion trajectory, and red spot illustrates the instantaneous intensity. **c** Flat-top spectrum for simulation. **d** Longitudinal axial (*z*-axis) intensity of FLFO at different propagating times *t* from appearance to disappearance, showing reciprocating propagation. Because the forward-propagating velocity *c* is much faster than the backward-propagating velocity −0.11c, the propagating time axis (vertical axis) is zoomed for the forward-propagations. For a very small Rayleigh dielectric sphere (2 nm radius) in the air, **e** induced longitudinal axial (*z*-axis) radiation-forces $\mathbf{F_{grad}}$, $\mathbf{F_{scat}}$, and $\mathbf{F_{net}}$ at the propagating time $t = 0$, and **f** induced axial (*z*-axis) ultrafast-reciprocating trapping forces $\mathbf{F_{net}}$ at different propagating times *t* from appearance to disappearance. The net force is $\mathbf{F_{net}} = \mathbf{F_{grad}} + \mathbf{F_{scat}}$. For a relatively big Rayleigh dielectric sphere (10 nm radius) in the air, **g** induced longitudinal axial (*z*-axis) radiation-forces $\mathbf{F_{grad}}$, $\mathbf{F_{scat}}$, and $\mathbf{F_{net}}$ at the propagating time $t = 0$, and **h** induced axial (*z*-axis) ultrafast-reciprocating pushing forces $\mathbf{F_{net}}$ at different propagating times *t* from appearance to disappearance.

continuous-wave Gaussian beams[46,47]. A study on the instantaneous radiation-forces produced by the pulsed Gaussian beams shows that, for long pulses (typically longer than 1 ps), stable optical trapping/manipulation like by the continuous-wave Gaussian beams can be obtained[48]. Figure 2f shows, because both the temporal chirp and the Rayleigh length are enlarged for a clear reciprocating FLFO, the temporal length of the reciprocating FLFO is around 5 ps (much longer than 1 ps), and consequently the induced radiation-forces $\mathbf{F_{scat}}$ and $\mathbf{F_{grad}}$ can be described well by the steady-state model given in the "Methods" section. Figure 5b schematically illustrates the FLFO experiences a reciprocating propagation trajectory within the extended Rayleigh length, in theory, which can produce a reciprocating radiation-force in space-time. Based on the clear reciprocating FLFO shown in Fig. 2f, the induced radiation-force is simulated. Figure 5c shows the flat-top spectrum of the pulse, and Fig. 5d shows the on-axis intensity distribution of the FLFO at different propagating times from its appearance (at around $t = -83$ ps) to its disappearance (at around $t = 83$ ps). Because of the subluminal velocity of the backward-propagation, the scale of the time axis (vertical axis) of Fig. 5d from $t = -75$ ps to $t = 75$ ps is reduced. When the total input energy is 1 mJ and the relative refractive index is $m = 1.511/1$, for a dielectric sphere radius $a = 2$ nm, Fig. 5e shows the on-axis gradient force $\mathbf{F_{grad}}$, scattering force $\mathbf{F_{scat}}$, and net force $\mathbf{F_{net}}$ ($\mathbf{F_{grad}} + \mathbf{F_{scat}}$) at the propagating time $t = 0$. The gradient force is significantly stronger than the scattering force, and the sphere can be trapped at the position $z = 0$ by the net force. Figure 5f shows the dynamics of the on-axis net force $\mathbf{F_{net}}$ at different propagating times from the appearance (at around $t = -83$ ps) to the disappearance (at around $t = 83$ ps), showing an ultrafast-reciprocating trapping force. When the radius of the dielectric sphere is increased from $a = 2$ nm to $a = 10$ nm, Fig. 5g, h show the on-axis radiation-forces at the propagating time $t = 0$ and the dynamics of the on-axis net force from $t = -83$ ps to $t = 83$ ps, respectively. The ultrafast-reciprocating trapping force is now changed into an ultrafast-reciprocating pushing force, because the scattering force is much stronger than the gradient force that dominates the net force. The two examples given in Fig. 5f, h are based on small particles (dipole) and show the induced reciprocating radiation-force that may bring some possibilities to advance ultrafast optical trapping or manipulation or acceleration. For large particles (multipoles), because backward-scattering forces exist[49], once it is combined with the reciprocating FLFO, an ultrafast-reciprocating trapping

force for multipoles might be possible, too. Besides that, the above simulation is based on a flat-top spectrum, as illustrated in Fig. 3, the spectral profile can influence the dynamics of the FLFO as well as the induced instantaneous radiation-force, of course, which can also provide opportunities for active control.

In addition to optical radiation pressure experiments, the ultra-intense traditional FLFO with superluminal or subluminal, accelerating or decelerating, and forward- or backward-propagating velocities recently have been used in laser-plasma physics applications like dephasingless/phase-locked laser-wakefield accelerator, arbitrary-velocity ionization wave generation, photon accelerator, laser-plasma amplifier, and so on[3–6,26,27,39,50]. The reciprocating FLFO introduced in this article, because of its characteristics, can further enhance the controllability of the laser pulse intensity in space-time and may also provide some opportunities in this field.

Conclusion

In this work, we have introduced a type of laser pulse intensity propagation or control, i.e., the reciprocating FLFO. Based on the recently reported FLFO (or named sliding focus) that is created by combining temporal chirp and longitudinal chromatism together[24–27], when both the Rayleigh length and the temporal chirp are dramatically increased, different from the previous result the produced FLFO would present a different motion form: flying forward–backward–forward along a straight-line in free space, showing a longitudinal-reciprocating trajectory. The existence condition of a clear reciprocating FLFO with a high longitudinal spatial resolution is also analyzed and introduced. In free space, a clear reciprocating FLFO has a light-speed forward-propagating velocity c and a subluminal backward-propagating velocity (typically $-0.11c < v_{\mathrm{FLFO}} < 0$), respectively. We have shown when this unique light is applied in radiation pressure simulations in the Rayleigh-scattering regime, for different particle radiuses an ultrafast-reciprocating trapping or pushing force can be induced in space-time. Moreover, in laser-plasma physics, the ultra-intense-reciprocating FLFO can further extend the performance of the traditional FLFO. All in all, this light may provide useful applications from nano-optics to high-field optics.

Methods

Numerical simulation of reciprocating FLFO. The propagation of the FLFO in a paraxial cylindrical coordinate system r-φ-z can be simulated by the Collins diffraction integral, and the optical field at the output of the ABCD system (i.e., spatial focusing and free propagation) is given by

$$E_{\mathrm{out}}(r_2,\varphi_2,z_2,\omega) = -\frac{i}{\lambda B}\iint E_{\mathrm{in}}(r_1,\varphi_1,z_1,\omega)\exp(ikS)r_1 dr_1 d\varphi_1 \tag{4}$$

with

$$S = z_2 + \frac{1}{2B}\left[Ar_1^2 - 2r_1 r_2\cos(\varphi_1-\varphi_2) + Dr_2^2\right] \tag{5}$$

$$\begin{bmatrix} A & B \\ C & D \end{bmatrix} = \begin{bmatrix} 1 & z_2 - z_1 \\ 0 & 1 \end{bmatrix}\begin{bmatrix} 1 & 0 \\ -\frac{1}{f(\omega)} & 1 \end{bmatrix} \tag{6}$$

where, $f(\omega)$ is the frequency-dependent focal length of the focusing optics (or a constant f for a focusing mirror), and z_1 and z_2 is the input and output on-axis position, respectively. The optical field at the input of the ABCD system is given by

$$\begin{aligned} E_{in}(r_1,\varphi_1,z_1,\omega) = A(\omega)\exp\left[i\tfrac{1}{2}\phi_2(\omega-\omega_0)^2\right] \\ \exp\left(-\tfrac{r_1^2}{w_{in}^2}\right)\exp\{-ik[z_1+\Delta z(r_1,\omega)]\}\end{aligned} \tag{7}$$

where, $A(\omega)$ is the spectral amplitude, ϕ_2 is GVD denoting the temporal chirp, w_{in} is the input beam waist, and $\Delta z(r_1,\omega)$ is the frequency-dependent wave-front denoting the longitudinal chromatism. For example, when a transmission telescope is used for generating the longitudinal chromatism, $\Delta z(r_1,\omega)$ is a quadratic function with respect to the transverse coordinate $\Delta z(r_1,\omega) = a(\omega){r_1}^2 + b$, where $a(\omega)$ is a frequency-dependent coefficient and b is a constant-coefficient[51–54], and accordingly PFC or named RGD of $\mathrm{GD}(r_1) = \alpha {r_1}^2$ will be produced in the near-field[25]. After the Fourier-transform, the output temporal optical field is given by

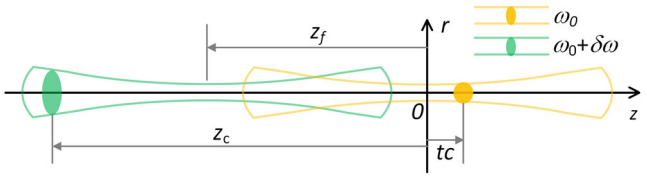

Fig. 6 Frequency- and time-dependent instantaneous propagation geometrics. The geometrical focus of the beam for the center frequency ω_0 is defined as the coordinate origin $z = 0$, and the time of the center frequency ω_0 arriving at $z = 0$ is defined as the propagating time origin $t = 0$. The geometrical focus of the beam for an arbitrary frequency $\omega_0 + \delta\omega$ is always at $z = z_f$. At a propagating time t, the center frequency ω_0 and an arbitrary frequency $\omega_0 + \delta\omega$ is instantaneously at $z = tc$ and $z = z_c$, respectively. The solid line and the solid spot denote the beam profile and the instantaneous position, respectively.

$$E_{\mathrm{out}}(r_2,\varphi_2,z_2,\tau) = \frac{1}{2\pi}\int E_{\mathrm{out}}(r_2,\varphi_2,z_2,\omega)\exp(i\omega\tau)d\omega \tag{8}$$

where τ is the local time. By choosing different propagating positions z_2, the dynamics of the FLFO at different propagating times t ($t = z/c$) can be obtained. The numerical simulation can show the dynamics of FLFOs well, however cannot give the mathematical influence of the Rayleigh length (i.e., normalized as $Z_R/|L_f|$) and the temporal chirp (i.e., normalized as L_c/L_f) directly. In this case, an approximately analytical description is also required.

Analytical description of reciprocating FLFO. In the theory of linear pulse propagation[55], the temporal profile of a deeply chirped pulse can be approximately described by its spectral profile, i.e., $I(t) \propto I(\omega)$. In this case, the dynamics of a deeply chirped FLFO in space-time can be approximately described by that in space-spectrum[56].

Figure 6 shows in the lateral plane of the coordinate system r-z, the space origin $z = 0$ is at the geometrical focus of the beam for the center frequency ω_0, and the time origin $t = 0$ is the time of the center frequency ω_0 arriving at the space origin $z = 0$. Then, the instantaneous position of the center frequency is at $z = tc$. In space, the longitudinal chromatism moves the geometrical focus of the beam for an arbitrary frequency $\omega = \omega_0 + \delta\omega$ to

$$z_f = 2cf^2\alpha\frac{\delta\omega}{\omega_0} \tag{9}$$

which is similar to Eq. (2) and given by Sainte-Marie et al.[24] and Jolly et al.[25]. In space-time, the temporal chirp moves the instantaneous position of an arbitrary frequency $\omega = \omega_0 + \delta\omega$ to

$$z_c = -\phi_2\delta\omega c + tc \tag{10}$$

where, the first term on the right side is the relative shift with respect to the center frequency [similar to Eq. (3)], and the second term on the right side is the instantaneous position of the center frequency. z_f is a function of frequency ω, while z_c is a function of both frequency ω and propagating time t. When $z_c = z_f$, different frequencies $\omega_f = \omega_0 + \delta\omega_f$ arrive at their geometrical foci at times

$$t_f = \left(2f^2\alpha\frac{1}{\omega_0} + \phi_2\right)\delta\omega_f \tag{11}$$

which shows a linear relationship between the appearance time of the backward-propagating FLFO with the frequency.

We assume the beam for every frequency has a Gaussian profile. Then, an arbitrary frequency ω at an arbitrary propagating time t is at an instantaneous position z_c and has an instantaneous beam radius w_z, which is given by

$$I(r,w_z) = I_0(\omega)\frac{w_0^2}{w_z^2}\exp\left[-2\frac{r^2}{w_z^2}\right] \tag{12}$$

with

$$w_z = w_0\sqrt{1+\left(\frac{z_c - z_f}{Z_R}\right)^2} \tag{13}$$

$$Z_R = \frac{1}{2}kw_0^2 \tag{14}$$

$$w_0 = \frac{2cf}{\omega w_{in}} \tag{15}$$

where, r is the transverse coordinate, $I_0(\omega)$ is the spectral intensity, w_0 is the beam waist, z_f is the geometrical focus (waist) position, Z_R is the Rayleigh length, k is the wavenumber, f is the focal length of the focusing optics, and w_{in} is the input beam

radius at the focusing optics. w_0 and Z_R are functions of frequency ω, while w_z and $I(r, w_z)$ are functions of both frequency ω and propagating time t.

From Eq. (12), the on-axis intensity distribution of FLFO can be simplified as

$$I_{\mathrm{FLFO}}(r=0,\omega,t)=I_0(\omega)\frac{1}{1+\left(\frac{z_c-z_f}{Z_R}\right)^2} \tag{16}$$

with

$$\begin{cases} -Z_R \le z_c(\omega_r,t)-z_f(\omega_r)<0, & \text{1st}-\text{forward} \\ z_c(\omega_f,t)-z_f(\omega_f)=0, & \text{backward} \\ 0<z_c(\omega_b,t)-z_f(\omega_b)\le Z_R, & \text{2nd}-\text{forward} \end{cases} \tag{17}$$

where, ω_r and ω_b are the lowest and the highest frequencies within the pulse bandwidth $\Delta\omega$, and ω_f is a variable frequency arriving at its geometrical focus at the time t_f during the backward-propagation and is governed by Eq. (11). Equations (16) and (17) show in three propagation stages FLFO overlaps with different frequencies, where $|z_c - z_f|$ has its minimum values and I_{FLFO} has the corresponding maximum values, i.e., the movement of FLFO. Equations (16) and (17) (and Fig. 1c) show: in the first forward-propagation, only the lowest-frequency ω_r ("red" light) enters its Rayleigh length [i.e., minimum $|z_c - z_f|$ only for ω_r, see Eq. (17)'s first formula], and FLFO overlaps with the lowest-frequency ω_r and propagates forwards at the velocity c; in the backward-propagation, different frequencies ω_f from the lowest one ω_r to the highest one ω_b arrive at their geometrical foci in turn [i.e., minimum $|z_c - z_f| = 0$ for different frequencies ω_f, see Eq. (17)'s second formula], and FLFO overlaps with different frequencies ω_f (from the lowest one ω_r to the highest one ω_b) at different propagating times t_f governed by Eq. (11) and propagates backwards at the velocity v_{FLFO} governed by Eq. (1); in the second forward-propagation, only the highest frequency ω_b ("blue" light) is still in its Rayleigh length [i.e., minimum $|z_c - z_f|$ only for ω_b, see Eq. (17)'s third formula], and FLFO overlaps with the highest frequency ω_b and propagates forwards at the velocity c. It is important to note that, as shown in Fig. 1, Eq. (17) is based on the case of positive temporal chirp $\phi_2 > 0$ (i.e., $L_c < 0$) and concave PFC $\alpha < 0$ (i.e., $L_f < 0$), if for the other case of negative temporal chirp $\phi_2 < 0$ (i.e., $L_c > 0$) and convex PFC $\alpha > 0$ (i.e., $L_f > 0$), the parameters ω_r and ω_b in Eq. (17) should be interchanged.

By substituting Eq. (17) with Eq. (16), once neglecting the overall spectral profile, the first forward-propagating FLFO has a position-dependent increasing peak intensity of [0.5, 1) from $z = |L_f|/2 - Z_R$ to $|L_f|/2$; the backward-propagating FLFO has a constant peak intensity of 1 from $z = |L_f|/2$ to $-|L_f|/2$; the second forward-propagating FLFO has a position-dependent decreasing peak intensity of (1, 0.5] from $z = -|L_f|/2$ to $-|L_f|/2 + Z_R$.

From Eqs. (16) and (17), the FWHM length ΔL of FLFO is derived and given by

$$\Delta L=\begin{cases} \left[\sqrt{3},\ 1\right)\frac{L_c}{L_c-L_f}2Z_R, & \text{1st}-\text{forward} \\ \frac{L_c}{L_c-L_f}2Z_R, & \text{backward} \\ \left(1,\ \sqrt{3}\right]\frac{L_c}{L_c-L_f}2Z_R, & \text{2nd}-\text{forward} \end{cases} \tag{18}$$

and Supplementary Information Note 4 gives the detailed derivations. The first and the third formulas of Eq. (18) show the forward-propagating FLFOs have variable lengths, which decreases and increases in the first and the second forward-propagations, respectively. While the second formula of Eq. (18) shows the backward-propagating FLFO has a constant length. This result agrees well with the simulation shown in Fig. 2f. Equation (18) also shows the lengths ΔL of FLFOs are proportional to a fixed product of $M \cdot Z_R$ where $M = L_c/(L_c - L_f)$, although the values of ΔL are slightly different in forward and backward propagations. Then, M and Z_R are key parameters to obtain a clear reciprocating FLFO.

Radiation-forces in the Rayleigh-scattering regime. Under the zeroth-order approximation of the continuous-wave Gaussian beam or a weakly focused continuous-wave Gaussian beam, the formulas of the scattering and gradient forces $\mathbf{F}_{\mathbf{scat}}$ and $\mathbf{F}_{\mathbf{grad}}$ exerted on a Rayleigh dielectric sphere in a steady-state are given by[43,45]

$$\vec{F}_{\mathrm{scat}}(x,y,z)=\hat{z}\left(\frac{n_2}{c}\right)\frac{8}{3}\pi(ka)^4a^2\left(\frac{m^2-1}{m^2+2}\right)^2 I(x,y,z) \tag{19}$$

and

$$\vec{F}_{\mathrm{grad}}(x,y,z)=\frac{2\pi n_2 a^3}{c}\left(\frac{m^2-1}{m^2+2}\right)^2\nabla I(x,y,z) \tag{20}$$

where, n_1 and n_2 are the refractive indexes of the dielectric sphere and the environment, $m = n_1/n_2$ is the relative refractive index, a is the radius of the dielectric sphere, $I(x, y, z)$ is the laser intensity, and $\nabla I(x, y, z)$ is the laser intensity gradient.

Data availability

The data that support the findings of this study are available from the corresponding author upon reasonable request.

Code availability

The code that support the findings of this study are available from the corresponding author upon reasonable request.

Received: 29 January 2021; Accepted: 29 March 2021;
Published online: 04 May 2021

References

1. Yin, X. & Zhang, X. Unidirectional light propagation at exceptional points. *Nat. Mater.* **12**, 175–177 (2013).
2. Yessenov, M., Bhaduri, B., Delfyett, P. J. & Abouraddy, A. F. Free-space optical delay line using space-time wave packets. *Nat. Commun.* **11**, 5782 (2020).
3. Turnbull, D. et al. Ionization waves of arbitrary velocity. *Phys. Rev. Lett.* **120**, 225001 (2018).
4. Howard, A. J. et al. Photon acceleration in a flying focus. *Phys. Rev. Lett.* **123**, 124801 (2019).
5. Palastro, J. P. et al. Dephasingless laser wakefield acceleration. *Phys. Rev. Lett.* **124**, 134802 (2020).
6. Caizergues, C., Smartsev, S., Malka, V. & Thaury, C. Phase-locked laser-wakefield electron acceleration. *Nat. Photon.* **14**, 475–479 (2020).
7. Hau, L. V., Harris, S. E., Dutton, Z. & Behroozi, C. Light speed reduction to 17 m per second in an ultracold atomic gas. *Nature* **397**, 594–598 (1999).
8. Gehring, G. M., Schweinsberg, A., Barsi, C., Kostinski, N. & Boyd, R. W. Observation of backward pulse propagation through a medium with a negative group velocity. *Science* **312**, 895–897 (2005).
9. Dolling, G., Enkrich, C., Wegener, M., Soukoulis, C. M. & Linden, S. Simultaneous negative phase and group velocity of light in a metamaterial. *Science* **312**, 892–894 (2005).
10. Baba, T. Slow light in photonic crystals. *Nat. Photon.* **2**, 465–473 (2008).
11. Boyd, R. W. & Gauthier, D. J. Controlling the velocity of light pulses. *Science* **326**, 1074–1077 (2009).
12. Simpson, T. T. et al. Nonlinear spatiotemporal control of laser intensity. *Opt. Express* **28**, 38516–38526 (2020).
13. Durnin, J., Miceli, J. J. & Eberly, J. H. Diffraction-free beams. *Phys. Rev. Lett.* **58**, 1499–1501 (1987).
14. Alexeev, I., Kim, K. Y. & Milchberg, H. M. Measurement of the superluminal group velocity of an ultrashort bessel beam pulse. *Phys. Rev. Lett.* **88**, 073901 (2002).
15. Siviloglou, G. A. & Christodoulides, D. N. Accelerating finite energy Airy beams. *Opt. Lett.* **32**, 979–981 (2007).
16. Siviloglou, G. A., Broky, J., Dogariu, A. & Christodoulides, D. N. Observation of accelerating Airy beams. *Phys. Rev. Lett.* **99**, 213901 (2007).
17. Siviloglou, G. A., Broky, J., Dogariu, A. & Christodoulides, D. N. Ballistic dynamics of Airy beams. *Opt. Lett.* **33**, 207–209 (2008).
18. Kaminer, I., Segev, M. & Christodoulides, D. N. Self-accelerating self-trapped optical beams. *Phys. Rev. Lett.* **106**, 213903 (2011).
19. Dolev, I., Kaminer, I., Shapira, A., Segev, M. & Arie, A. Experimental observation of self-accelerating beams in quadratic nonlinear media. *Phys. Rev. Lett.* **108**, 113903 (2012).
20. Kaminer, I., Bekenstein, R., Nemirovsky, J. & Segev, M. Nondiffracting accelerating wave packets of Maxwell's equations. *Phys. Rev. Lett.* **108**, 163901 (2012).
21. Schley, R. et al. Loss-proof self-accelerating beams and their use in non-paraxial manipulation of particles' trajectories. *Nat. Commun.* **11**, 261–267 (2015).
22. Efremidis, N. K., Chen, Z., Segev, M. & Christodoulides, D. N. Airy beams and accelerating waves: an overview of recent advances. *Optica* **6**, 686–701 (2019).
23. Chong, A., Renninger, W. H., Christodoulides, D. N. & Wise, F. W. Airy–Bessel wave packets as versatile linear light bullets. *Nat. Photon.* **4**, 103–106 (2010).
24. Sainte-Marie, A., Gobert, O. & Quéré, F. Controlling the velocity of ultrashort light pulses in vacuum through spatio-temporal couplings. *Optica* **4**, 1298–1304 (2017).
25. Jolly, S. W., Gobert, O., Jeandet, A. & Quéré, F. Controlling the velocity of a femtosecond laser pulse using refractive lenses. *Opt. Express* **28**, 4888–4897 (2020).
26. Froula, D. H. et al. Spatiotemporal control of laser intensity. *Nat. Photon.* **12**, 262–265 (2018).
27. Froula, D. H. et al. Flying focus: Spatial and temporal control of intensity for laser-based applications. *Phys. Plasmas* **26**, 032109 (2019).
28. Kondakci, H. E. & Abouraddy, A. F. Diffraction-free space-time beams. *Nat. Photon.* **11**, 733–740 (2017).
29. Kondakci, H. E. & Abouraddy, A. F. Airy wavepackets accelerating in space-time. *Phys. Rev. Lett.* **120**, 163901 (2018).
30. Bhaduri, B., Yessenov, M. & Abouraddy, A. F. Meters-long propagation of diffraction-free space-time light sheets. *Opt. Express* **26**, 20111–20121 (2018).

31. Kondakci, H. E. & Abouraddy, A. F. Optical space-time wave packets having arbitrary group velocities in free space. *Nat. Commun.* **10**, 929 (2019).
32. Bhaduri, B., Yessenov, M. & Abouraddy, A. F. Space-time wave packets that travel in optical materials at the speed of light in vacuum. *Optica* **6**, 139–146 (2019).
33. Yessenov, M. & Abouraddy, A. F. Changing the speed of optical coherence in free space. *Opt. Lett.* **44**, 5125–5128 (2019).
34. Yessenov, M. & Abouraddy, A. F. Accelerating and decelerating space-time optical wave packets in free space. *Phys. Rev. Lett.* **125**, 233901 (2020).
35. Li, Z. & Kawanaka, J. Velocity and acceleration freely tunable straight-line propagation light bullet. *Sci. Rep.* **10**, 11481 (2020).
36. Li, Z. & Kawanaka, J. Optical wave-packet with nearly-programmable group velocities. *Commun. Phys.* **3**, 211 (2020).
37. Valtna, H., Reivelt, K. & Saari, P. Methods for generating wideband localized waves of superluminal group velocity. *Opt. Commun.* **278**, 1–7 (2007).
38. Li, Z. & Miyanaga, N. Theoretical method for generating regular spatiotemporal pulsed-beam with controlled transverse-spatiotemporal dispersion. *Opt. Commun.* **432**, 91–96 (2019).
39. Franke, P. et al. Measurement and control of large diameter ionization waves of arbitrary velocity. *Opt. Express* **27**, 31978–31988 (2019).
40. Ashkin, A. Acceleration and trapping of particles by radiation pressure. *Phys. Rev. Lett.* **24**, 156–159 (1970).
41. Ashkin, A. Tapping of atoms by resonance radiation pressure. *Phys. Rev. Lett.* **40**, 729–732 (1978).
42. Ashkin, A. Applications of laser radiation pressure. *Science* **210**, 4474 (1980).
43. Ashkin, A., Dziedzic, J. M., Bjorkholm, J. E. & Chu, S. Observation of a single-beam gradient force optical trap for dielectric particles. *Opt. Lett.* **11**, 288–290 (1986).
44. Ashkin, A. Optical trapping and manipulation of neutral particles using lasers. *Proc. Natl Acad. Sci. USA* **94**, 4853–4860 (1997).
45. Harada, Y. & Asakura, T. Radiation forces on a dielectric sphere in the Rayleigh scattering regime. *Opt. Commun.* **124**, 529–541 (1996).
46. Ambardekar, A. A. & Li, Y. Q. Optical levitation and manipulation of stuck particles with pulsed optical tweezers. *Opt. Lett.* **30**, 1797–1799 (2005).
47. Deng, J. L., Wei, Q., Wang, Y. Z. & Li, Y. Q. Numerical modeling of optical levitation and trapping of the stuck particles with a pulsed optical tweezers. *Opt. Express* **13**, 3673–3680 (2006).
48. Wang, L.-G. & Zhao, C. H.-L. Dynamic radiation force of a pulsed Gaussian beam acting on a Rayleigh dielectric sphere. *Opt. Express* **15**, 10615–10621 (2007).
49. Chen, J., Ng, J., Lin, Z. & Chan, C. T. Optical pulling force. *Nat. Photon.* **5**, 531–534 (2011).
50. Turnbull, D. et al. Flying focus and its application to plasma-based laser amplifiers. *Plasma Phys. Control. Fusion* **61**, 014022 (2018).
51. Bor, Z. Distortion of femtosecond laser pulses in lenses and lens systems. *J. Mod. Opt.* **35**, 1907–1918 (1988).
52. Bor, Z. Distortion of femtosecond laser pulses in lenses. *Opt. Lett.* **14**, 119–121 (1989).
53. Li, Z. & Kawanaka, J. Efficient method for determining pulse-front distortion in an ultra-intense laser. *J. Opt. Soc. Am. B* **37**, 2595–2603 (2020).
54. Jolly, S. W., Gobert, O. & Quéré, F. Spatio-temporal characterization of ultrashort laser beams: a tutorial. *J. Opt.* **22**, 103501 (2020).
55. Siegman, A. E. in *Lasers*. Ch. 9 (University Science Books, 1986).
56. Chong, A., Kuznetsova, L. & Wise, F. W. Theoretical optimization of nonlinear chirped-pulse fiber amplifiers. *J. Opt. Soc. Am. B* **24**, 1815–1823 (2007).

Acknowledgements

This work was supported by the JST-Mirai Program, Japan, under contract JPMJMI17A1.

Author contributions

Z.L. developed the concept, derived the equations, performed the simulations, and wrote the manuscript. Y.G. commented on the application part, and J.K. commented on the optical propagation part. All authors discussed the results and commented on the manuscript.

Competing interests

The authors declare no competing interests.

Additional information

Supplementary information The online version contains supplementary material available at https://doi.org/10.1038/s42005-021-00590-8.

Correspondence and requests for materials should be addressed to Z.L.

Reprints and permission information is available at http://www.nature.com/reprints

Publisher's note Springer Nature remains neutral with regard to jurisdictional claims in published maps and institutional affiliations.